

**Naval Surface Warfare Center
Carderock Division**
West Bethesda, MD 20817-5700



NSWCCD-50-TR-2012/032

June 2012

Hydromechanics Department Report

**WAVE FIELD CHARACTERIZATION USING DUAL-
POLARIZED PULSE-DOPPLER X-BAND RADAR**



By

Erin E. Hackett, Anne M. Fullerton, Craig F. Merrill, and Thomas C. Fu



Approved for public release; distribution unlimited.

REPORT DOCUMENTATION PAGE			Form Approved OMB No. 0704-0188	
Public reporting burden for this collection of information is estimated to average 1 hour per response, including the time for reviewing instructions, searching existing data sources, gathering and maintaining the data needed, and completing and reviewing this collection of information. Send comments regarding this burden estimate or any other aspect of this collection of information, including suggestions for reducing this burden to Department of Defense, Washington Headquarters Services, Directorate for Information Operations and Reports (0704-0188), 1215 Jefferson Davis Highway, Suite 1204, Arlington, VA 22202-4302. Respondents should be aware that notwithstanding any other provision of law, no person shall be subject to any penalty for failing to comply with a collection of information if it does not display a currently valid OMB control number. PLEASE DO NOT RETURN YOUR FORM TO THE ABOVE ADDRESS.				
1. REPORT DATE (DD-MM-YYYY) June 2012		2. REPORT TYPE Final		3. DATES COVERED (From - To) July 2010 - June 2012
4. TITLE AND SUBTITLE Wave Field Characterization using Dual-Polarized Pulse-Doppler X-band Radar		5a. CONTRACT NUMBER N0001411WX20753, N0001410WX21167, N0001412WX20711		
		5b. GRANT NUMBER		
		5c. PROGRAM ELEMENT NUMBER 0603236N, 0602236N		
		5d. PROJECT NUMBER		
6. AUTHOR(S) Erin E. Hackett, Anne M. Fullerton, Craig F. Merrill, and Thomas C. Fu		5e. TASK NUMBER		
		5f. WORK UNIT NUMBER 11-1-5800-363, 10-1-5800-328, 1000005395050100		
7. PERFORMING ORGANIZATION NAME(S) AND ADDRESS(ES) AND ADDRESS(ES) Naval Surface Warfare Center Carderock Division 9500 Macarthur Boulevard West Bethesda, MD 20817-5700		8. PERFORMING ORGANIZATION REPORT NUMBER NSWCCD-50-TR-2012/032		
9. SPONSORING / MONITORING AGENCY NAME(S) AND ADDRESS(ES) Dr. Paul E. Hess III, Office of Naval Research One Liberty Center 875 N. Randolph Street Suite 1425 Arlington, VA 22203-1995		10. SPONSOR/MONITOR'S ACRONYM(S) ONR		
		11. SPONSOR/MONITOR'S REPORT NUMBER(S)		
12. DISTRIBUTION / AVAILABILITY STATEMENT Approved for public release; distribution unlimited.				
13. SUPPLEMENTARY NOTES				
14. ABSTRACT Use of radar as a remote sensing technique for measurement of ocean surface waves presents many advantages over conventional point sensors, such as wave buoys or wave gauges. One such advantage is the ability to obtain phase-resolved wave field measurements over vast areas and at locations far from the sensor. As the use of radar for wave measurements becomes more widespread, it is important to understand the dependence and sensitivity of the extracted wave parameters on the characteristics of the radar and the scatterers. To examine such issues, experiments were performed offshore of the Scripps Institution of Oceanography(SIO) pier in July 2010. Radar				
15. SUBJECT TERMS Sea Clutter, Coherent Radar, Ocean Surface Waves, Sea State Measurements				
16. SECURITY CLASSIFICATION OF:		17. LIMITATION OF ABSTRACT	18. NO. OF PAGES 30+vi+ii	19a. RESPONSIBLE PERSON Erin Hackett
a. REPORT UNCLASSIFIED	b. ABSTRACT UNCLASSIFIED			c. THIS PAGE UNCLASSIFIED

20120716028

14. ABSTRACT (continued)

measurements of the wave field were performed with dual-polarized high-resolution X-band pulse-Doppler radar at low grazing angles along with two independent measurements of the surface waves using conventional sensors. These data were taken in low sea states so that effects associated with breaking waves were minimized.

Comparison between RCS and Doppler modulations show peak values occurring in-phase, in contrast with tilt modulation theory. Spectral comparisons between Doppler-based and RCS-based spectra show that Doppler-based spectra demonstrate a greater sensitivity to swell-induced modulations. RCS-based spectra show greater sensitivity to small-scale modulations, and they equally capture energy at the wind wave peak. Comparison with conventional sensor data reveals Doppler estimates of peak period are more favorable than RCS-based estimates, while higher order period statistics are fairly accurate and similar. Radar-based significant wave heights are generally lower than buoy-based values, and contain nontrivial variability of ~33%. Comparisons between HH and VV polarization data are also examined.

CONTENTS

ABSTRACT	1
ACKNOWLEDGEMENTS.....	1
ADMINISTRATIVE INFORMATION	1
INTRODUCTION	1
EXPERIMENTS.....	3
CONVENTIONAL WAVE FIELD MEASUREMENTS.....	3
RADAR MEASUREMENTS	4
METHODS.....	5
DOPPLER-BASED SEA SURFACE ELEVATION SPECTRA	6
RCS-BASED SEA SURFACE ELEVATION SPECTRA	9
RESULTS.....	10
DOPPLER AND RCS COMPARISONS IN THE SPATIOTEMPORAL DOMAIN.....	11
DOPPLER AND RCS COMPARISONS IN FOURIER DOMAIN	15
COMPARISON WITH CONVENTIONAL SENSOR DATA.....	18
SUMMARY AND DISCUSSION.....	25
REFERENCES	29

FIGURES

Figure 1. Senix array installed on the Parker.....	4
Figure 2. Radar setup at the end of the SIO pier.	5
Figure 3. Wind speed (—) and direction (×) during the experiments. Solid triangles indicate periods of radar data collection.....	6
Figure 4. Sample spatiotemporal image of VV Doppler velocity with the mean value removed. Data is for run 246.....	7
Figure 5. Average 2-D power spectral density of VV Doppler velocities a) before dispersion curve filtering, and b) after filtering (Eqn. 2). The dashed white line is the dispersion relationship for surface gravity waves (Eqn. 3). Data is for run 246.....	9
Figure 6. Spatiotemporal image of a) RCS for HH polarization and b) RCS for VV polarization for the same time period as Figure 4.	10
Figure 7. Comparison of VV RCS-based wave height spectra computed from 2-D spectra that were first integrated over radian frequency or first integrated over wavenumber to obtain 1-D frequency spectra.....	11
Figure 8. Mean cross-correlation function between VV Doppler velocities and (black) VV RCS and (red) HH RCS for dataset 246.	12
Figure 9. Maximum correlation coefficients between VV Doppler, and (red) HH RCS and (black) VV RCS versus range for datasets (a) 252, (b) 259, and (c) 268.	14
Figure 10. Nominal correlation coefficient between VV Doppler, and VV and HH RCS versus wind speed.....	15
Figure 11. Spectral comparisons between Doppler- and RCS-based sea surface elevation spectra for datasets 236, 246, 250, and 252 (dataset denoted in each subfigure title).....	16
Figure 12. Spectral comparisons between Doppler- and RCS-based sea surface elevation spectra for datasets 254, 258, 259, and 263 (dataset denoted in each subfigure title).....	17
Figure 13. Spectral comparisons between Doppler- and RCS-based sea surface elevation spectra for datasets 265, 267, 268, 269, and 272 (dataset denoted in each subfigure title).	18
Figure 14. Comparison of buoy, (Senix) array, Doppler, and RCS wave height spectra for runs 236, 246, 250, and 252 (dataset denoted in each subfigure title).	20
Figure 15. Comparison of buoy, (Senix) array, Doppler, and RCS wave height spectra for runs 254, 258, 259, and 263 (dataset denoted in each subfigure title).	21
Figure 16. Comparison of buoy, Senix array, Doppler, and RCS wave height spectra for runs 265, 267, 268, 269, and 272 (dataset denoted in each subfigure title).	22
Figure 17. Time histories of (a) peak period, (b) mean period, and (c) zero-crossing period as computed from Doppler-, buoy-, array-, and RCS-based spectra.	23
Figure 18. Differences between buoy measured periods and the other sensors for (a) peak period, (b) mean period, and (c) zero-crossing period.	24

Figure 19. (a) Time history of significant wave height as measured by the buoy, array,
Doppler, and RCS. (b) Difference between buoy measured significant wave height and
that measured by Doppler, RCS, and ultrasonic array versus wind speed. 26

TABLES

Table 1. Relevant characteristics associated with sea clutter measurements.	5
Table 2. Maximum and minimum correlation coefficients for all range bins and lags, and overall maximum value and associated lag.	13
Table 3. Date and time of radar, buoy, and Senix array wave measurements that are used for comparisons. All times are in UTC.	19
Table 4: Mean and RMS of differences between buoy measured and array, Doppler, and RCS measured wave statistics.	24

INTERNATIONAL SYSTEM OF UNITS (SI) CONVERSION LIST

U.S. CUSTOMARY

METRIC EQUIVALENT

1 inch (in)	25.4 millimeter (mm), 0.0254 meter (m)
1 foot (ft)	0.3048 meter (m)
1 pound-mass (lbm)	0.4536 kilograms (kg)
1 pound-force (lbf)	4.448 Newtons (N)
1 foot-pound-force (ft-lbf)	1.3558 Newton-meters (N-m)
1 foot per second (ft/s)	0.3048 meter per second (m/s)
1 knot (kt)	1.6878 feet per second (ft/s) 0.5144 meter per second (m/s)
1 horsepower (hp)	0.7457 kilowatts (kW)
1 long ton (LT)	1.016 tonnes 1.016 metric tons 1016 kilograms (kg) 2240 pounds
1 inch water (60F)	248.8 Pascals (Pa)

(THIS PAGE INTENTIONALLY LEFT BLANK)

ABSTRACT

Use of radar as a remote sensing technique for measurement of ocean surface waves presents many advantages over conventional point sensors, such as wave buoys or wave gauges. One such advantage is the ability to obtain phase-resolved wave field measurements over vast areas and at locations far from the sensor. As the use of radar for wave measurements becomes more widespread, it is important to understand the dependence and sensitivity of the extracted wave parameters on the characteristics of the radar and the scatterers. To examine such issues, experiments were performed offshore of the Scripps Institution of Oceanography (SIO) pier in July 2010. Radar measurements of the wave field were performed with dual-polarized high-resolution X-band pulse-Doppler radar at low grazing angles along with two independent measurements of the surface waves using conventional sensors. These data were taken in low sea states so that effects associated with breaking waves were minimized.

Comparison between RCS and Doppler modulations show peak values occurring in-phase, in contrast with tilt modulation theory. Spectral comparisons between Doppler-based and RCS-based spectra show that Doppler-based spectra demonstrate a greater sensitivity to swell-induced modulations. RCS-based spectra show greater sensitivity to small-scale modulations, and they equally capture energy at the wind wave peak. Comparison with conventional sensor data reveals Doppler estimates of peak period are more favorable than RCS-based estimates, while higher order period statistics are fairly accurate and similar. Radar-based significant wave heights are generally lower than buoy-based values, and contain nontrivial variability of ~33%. Comparisons between HH and VV polarization data are also examined.

ACKNOWLEDGEMENTS

The authors would like to acknowledge the following people for their assistance during the field work: Eric Terrill and the other members of the Coastal Observing Research and Development Center at the Scripps Institution of Oceanography; Kristine Beale, Peter Stanton, and Don Wyatt from SAIC, Inc.; and Richard Pokrass from Sensor Concepts Inc. The authors would also like to recognize Andy Smith and Shaun Simmons, NSWCCD Code 70, for their participation and assistance with the tests. This research was supported by the Office of Naval Research under program manager Paul E. Hess III. We appreciate Paul's encouragement and support for this effort.

ADMINISTRATIVE INFORMATION

The work described in this report was performed by the Science and Technology Development Branch of the Resistance and Propulsion Division (Code 583) of the Hydromechanics Department at the Naval Surface Warfare Center, Carderock Division (NSWCCD). The work was performed under program elements 0603236N and 0602236N, work requests N0001411WX20753, N0001410WX21167, and N0001412WX20711, and work unit numbers 11-1-5800-363, 10-1-5800-328, and network activity number 1000005395050100.

INTRODUCTION

Use of radar as a remote sensing technique for measurement of ocean surface waves presents many advantages over conventional point sensors, such as wave buoys or wave gauges. One such advantage is the ability to obtain phase-resolved wave field measurements over vast areas and at locations far from the sensor, which provides needed wave data for applications such as tsunamis, rogue waves, wave evolution and development during storms, and onset of wind-

induced chop. Although techniques to extract wave parameters from radar measurements have been evolving over the past several decades [1, 2] along with our understanding of the scatterers that contribute to sea clutter [3], they still have limited accuracy and reliability. The primary reason is due to the large number of factors that sea clutter depends on, both radar parameters as well as sea characteristics. The backscattered signal from the sea surface depends to varying extents on radar characteristics such as radar wavelength, polarization, frequency band, grazing angle, and pulse duration. Sea characteristics such as surface roughness (capillary waves), wave height, wave period, wave direction, bimodality, bidirectionality, and steepness/breaking also impact the characteristics of the return signal. And finally, aspects associated most directly with the interaction of the electromagnetic waves with the sea surface also come into play such as shadowing, multibounce, and multipath.

Fluctuations of the return signal amplitude or intensity are generally divided into “fast” and “slow” types. The former are primarily the Bragg-scale scatterers, i.e., capillary waves, ripples, or surface roughness, which have a random character similar to noise, and re-radiate energy back to the antenna incoherently [4]. The slow fluctuations are related to the longer ocean surface waves, both swell and wind seas. These slow fluctuations are primarily attributed to tilt and hydrodynamic modulation of the background signal, which is produced by the mean intensity level of the fast scatterers [5]. In addition, for low grazing angles, shadowing and multipath also strongly modulate the signal [6, 7]. At first order, this characterization of the backscattered signal is accurate; however, there are clearly contributions to the return signal that are not associated with modulation of the dominant Bragg scattering, such as scattering from wave facets [8] or intermediate-scale waves [9]. These other contributors to the backscatter result in discrepancies between two-scale (composite) models [10] and experimental data, in addition to other unaccounted for factors that can cause variations in the signal amplitude such as multipath. These discrepancies are usually further highlighted when differences between various polarization returns cannot be explained solely by modulation of Bragg scattering [3, 9].

Coherent radars measure both the amplitude and phase of the return signal. The phase contains information about the velocities of the scatterers. These Doppler velocities are modulated by the underlying surface gravity waves, and wave statistics can be extracted from them [11-13]. The Doppler velocity also consists of many contributors including, the phase speed of capillary waves, surface currents of all sources, and the surface wave orbital velocities. Thus, the instantaneous Doppler velocity is complex, but its slow (order seconds) time variation is assumed to be primarily attributable to variations in the orbital velocities [11-13]. An advantage of using the velocity (phase) signal rather than the backscatter intensity is that there is a known relationship between wave orbital velocities and wave height based on linear wave theory. Thus, in principal, one can compute wave heights from a Doppler velocity spectrum without use of empirical relationships as is required for intensity measurements [14]. Consequently, it is speculated that wave height measurements based on Doppler velocities should be more accurate than those based on intensity.

As the use of radar for wave measurements becomes more widespread, it is important to understand the dependence and sensitivity of the extracted wave parameters on the characteristics of the radar and the (ocean surface) scatterers. This improved understanding could lead to a determination of an ideal radar system for wave measurements. In the interim, it provides insight as to how measurements are affected by variations in radar and sea state parameters. To examine these issues, experiments were performed offshore of the Scripps Institution of Oceanography (SIO) pier in July 2010. Radar measurements of the wave field were performed with a dual-polarized high-resolution X-band pulse-Doppler radar at low grazing angles along with two

independent measurements of the surface waves using conventional sensors. Two conventional sensors were used because they provide a measure of the non-stationarity and inhomogeneity of the wave field as a reference point for comparison with the radar measurements. Wave height spectra are computed using phase and amplitude of the radar return signal, as well as from water velocity and sea surface height data acquired with the conventional sensors. The shapes of wave height spectra based-on vertical-transmit and vertical-receive (VV) radar cross section (RCS), horizontal-transmit and horizontal-receive (HH) RCS, and VV Doppler are compared and discussed, as well as cross-correlation functions between them. All spectra and resulting wave parameters (e.g., wave period and wave height) are compared with those obtained with the conventional sensors. These data were taken in low sea states so that effects associated with breaking waves were minimized to permit evaluation of differences associated only with the geometries of the waves, as opposed to effects associated with spray and foam. The data also highlight some of the differences in returns between HH and VV polarizations.

EXPERIMENTS

From 26-30 July 2010, experiments were performed offshore of the Scripps Institution of Oceanography (SIO) pier, which is located at 32.87 deg north and 117.26 deg west and is oriented at 277 deg to true north. The experiments involved measurement of sea clutter using a linear FM homodyne X- and Ku-band instrumentation radar. In addition, two independent measurements of the sea state were performed using conventional sensors to evaluate the time and space variability of the local wave field, and to provide measurements against which the radar results could be compared. One source was an array of Senix ultrasonic distance sensors that were installed aboard a 7.6 m (25 ft) Parker Craft (hereafter referred to as the Parker). The second was a miniature directional wave buoy deployed from the Parker. This section reviews pertinent details of these experiments, but the reader is referred to a report by Hackett et al. [15] for a comprehensive description of the experiments and instrumentation.

CONVENTIONAL WAVE FIELD MEASUREMENTS

Three Senix TSPC-15S-232 ultrasonic distance sensors were mounted on booms extending from the Parker. The configuration of these sensors on the Parker is shown in Figure 1. This Senix array measured height above the water at 20 Hz at three different x , y , and z locations with an accuracy of ± 0.25 mm over a range of ± 3 m. The Parker drifted near the region of interest (i.e., close to but outside the area illuminated by the radar) when collecting sea state data. The data was motion corrected using measurements from a Crossbow, model NAV440, inertial measurement unit (IMU), which collected data synchronously with the Senix measurements at 20 Hz. The IMU measured angle (e.g., roll, pitch, yaw), angular rate, and acceleration at resolutions of 0.02 deg, 0.02 deg s^{-1} , and 0.5 mg (milli-g), respectively. The corresponding maximum ranges were ± 180 deg (± 90 deg for pitch), ± 200 deg s^{-1} , and ± 4 g. The motion-corrected water level measurements were used to estimate directional wave spectra using a phase-path-time difference method from which various wave statistics can be computed, including one-dimensional (1-D) frequency spectra, significant wave height, and peak period [16-18].

A GPS-based miniature directional wave buoy was deployed from the Parker and drifted near the region of interest until recovered at the end of each test day. The buoy measured water velocities, which were processed onboard using linear wave theory to obtain (20-minute averaged) sea surface elevation spectra from which other wave statistics were computed. The spectral data, buoy position, GPS time, mean period and direction, peak period and direction, and significant wave height were then transmitted to a shore-based computer via wireless

communications. The original velocity time series were discarded. These data were sampled approximately every 30 min while the buoy was deployed.

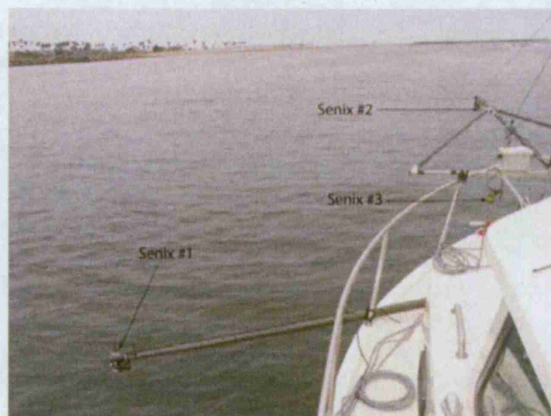


Figure 1. Senix array installed on the Parker.

In addition, tidal water level, wind speed, and wind direction data were collected by permanent sensors located at the SIO pier. Tidal data were obtained from tidal station 9410230, and wind speed and direction from an anemometer at the end of the SIO pier. The wind speed and direction data was provided hourly, while the tidal data was in 6 min increments. The anemometer was located approximately 20 m above mean sea level.

RADAR MEASUREMENTS

A 1.22 m (4 ft) diameter circular (dish) antenna was mounted at the end of the SIO pier approximately 14 m above the sea surface as shown in Figure 2. The 2-way 3db beam width was about 1.2 deg in both elevation and azimuth. Measurements were performed at X- and Ku-bands with both VV and HH polarizations; however, this paper focuses on the X-band data. On average, the distance to the first radar range bin was approximately 820 m at a grazing angle of 1 deg. The center radar frequency was 9.3 GHz, with a bandwidth of 0.5 GHz in 2048 frequency steps, which corresponds to a range bin size of 30 cm, and a total range extent of 614 m. For each data collection period, the radar antenna remained fixed at a set azimuth (i.e., it did not rotate), where data was collected at a pulse repetition frequency (PRF) of 800 Hz. The associated Doppler velocity range was $\pm 6.5 \text{ m s}^{-1}$. The antenna was pointed primarily into the direction of wave propagation, which was determined visually. Post-processing and comparison with peak wave directions measured by the wave buoy indicate that for the majority of the tests the radar-look direction was not more than 25 deg offset from the peak wave direction. Each dataset collected was 10-20 minutes in duration, and the average water depth in the measurement region was 48 m. Over the course of the experiments, 13 different data sets were collected and the wind speeds and directions during these times are shown in Figure 3. Table 1 provides the specific values for pertinent characteristics for each run: distance to the first range bin (R), radar azimuth (θ_r), tidal water level above MLLW (h_t), antenna height above the water surface (H), grazing angle (θ_g), peak wave direction (θ_p) as reported by the wave buoy, difference in radar azimuth and peak wave direction ($\Delta\theta = |\theta_p - \theta_r|$), wind direction (θ_w), and wind speed (U_w).

METHODS

The radar data are used to obtain sea surface elevation spectra. These spectra are obtained using both the phase (Doppler) and amplitude (RCS) from the radar return signal. In this section, the methods used to obtain sea surface elevation spectra from the RCS and Doppler measurements are described.

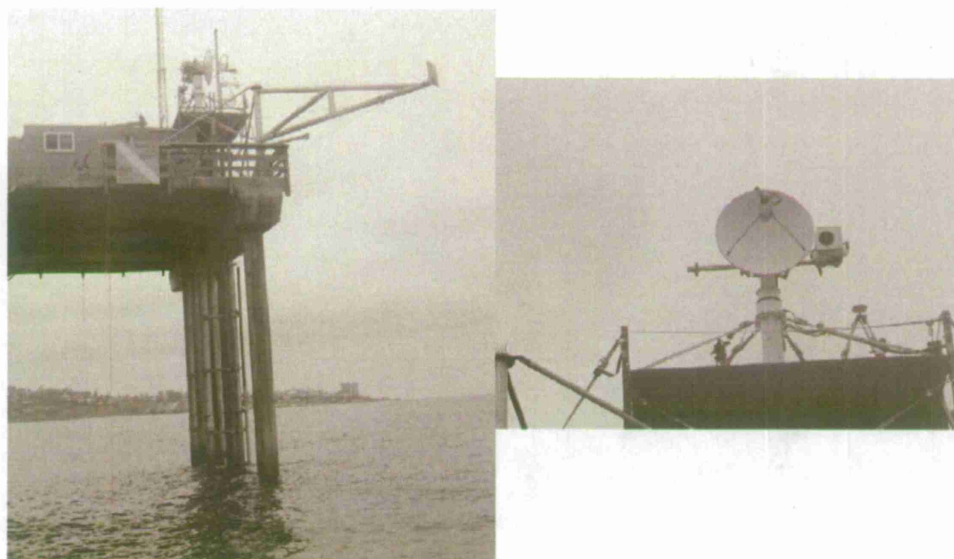


Figure 2. Radar setup at the end of the SIO pier.

Table 1. Relevant characteristics associated with sea clutter measurements.

Run	R (m)	θ_r (deg)	h_t (m)	H (m)	θ_g (deg)	θ_p (deg)	$\Delta\theta$ (deg)	θ_w (deg)	U_w (m/s)
236	674.25	272	1.165	13.845	1.18	281.00	9.00	291.00	2.80
246	803.76	269.4	0.725	14.285	1.02	282.00	12.60	297.00	3.90
250	803.76	No data	0.536	14.474	1.03	281.00	N/A	298.00	5.30
252	803.76	295	1.065	13.945	0.99	277.00	18.00	353.00	4.80
254	915.28	295	1.218	13.792	0.86	228.00	67.00	345.00	3.80
258	915.28	275.65	1.135	13.875	0.87	288.00	12.35	311.50	3.40
259	915.28	275.86	0.974	14.036	0.88	231.00	44.86	299.00	3.90
263	803.76	283.15	0.612	14.398	1.03	252.00	31.15	294.00	3.70
265	803.76	267.9	0.649	14.361	1.02	285.00	17.10	301.00	1.90
267	791.78	282.25	1.172	13.838	1.00	285.00	4.06	323.00	1.20
268	803.76	285.33	1.250	13.760	0.98	285.00	0.33	317.00	2.25
269	815.77	300.5	1.132	13.878	0.97	296.00	4.5	296.00	3.90
272	806.17	317.51	0.910	14.100	1.00	296.00	21.51	294.00	3.90

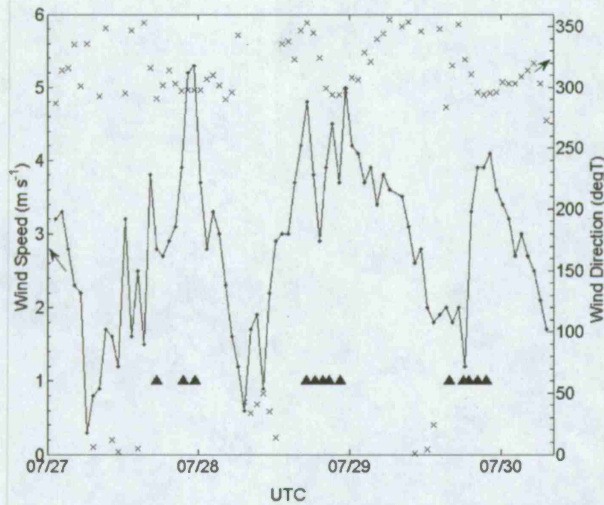


Figure 3. Wind speed (—) and direction (x) during the experiments. Solid triangles indicate periods of radar data collection.

DOPPLER-BASED SEA SURFACE ELEVATION SPECTRA

Raw radar data is first range-resolved. Pulse-pair processing [e.g., 19] is then applied to the phase of the return signal and converted to Doppler velocity using:

$$v(r, t) = -\frac{\partial \phi(r, t)}{\partial t} \frac{1}{2k_r \cos \theta_g} \quad (1)$$

where, ϕ is the phase, r is range, t is time, θ_g is the grazing angle, and k_r is the radar wavenumber. To reduce noise and increase sensitivity, for each range bin, a boxcar filter is subsequently applied to the time series of Doppler velocity. The filter consists of 256 points, which, with a PRF of 800 Hz, corresponds to 0.32 s. This filtering reduces high frequency noise without impacting variations of Doppler velocity related to surface gravity waves because the averaging time period is much less than the surface gravity wave period. Note that Doppler velocities computed from pulse-pair processing are equivalent to the first moment (mean) of the Doppler velocity spectrum of each range bin, when processed with more conventional fast-Fourier transform (FFT) Doppler processing [19]. A sample ~20 s spatiotemporal image of Doppler velocity with the mean value removed is shown in Figure 4. The mean value is an offset associated with steady scatterer velocities such as phase-speeds of Bragg-scale/capillary waves and surface currents. The structure and pattern associated with gravity waves is evidenced by the sloped lines of alternating high and low velocities. There are wide bands at a spacing of approximately 150 m and 10 s, which are associated with the swell. There are also narrower bands superimposed on top of these bands at an approximately 4 s and 30 m spacing, which are associated with the wind waves. The slopes of these two bands are the associated phase speeds of the waves. Most of the velocity values are within $\pm 50 \text{ cm s}^{-1}$, i.e., on the order of orbital velocities, but there are clearly larger values that appear predominantly near the crests of the waves. Some of these values may be associated with phase speeds of breaking waves [20], but clearly not all can be associated with breaking because very little breaking was visually observed. These velocity spikes are likely to also be associated

with coherent scattering off of facets on the crest of the waves, perhaps from intermediate-scale (wavelength ~ 1 m) waves that would have phase speeds on the order of 1 m s^{-1} [9]. This type of coherent scattering is even observed (albeit less frequently) in the absence of Bragg-scattering, when measurements were performed on a glassy sea surface ($U_w \sim 1 \text{ m s}^{-1}$) that still contained some low amplitude swell/decaying wind seas.

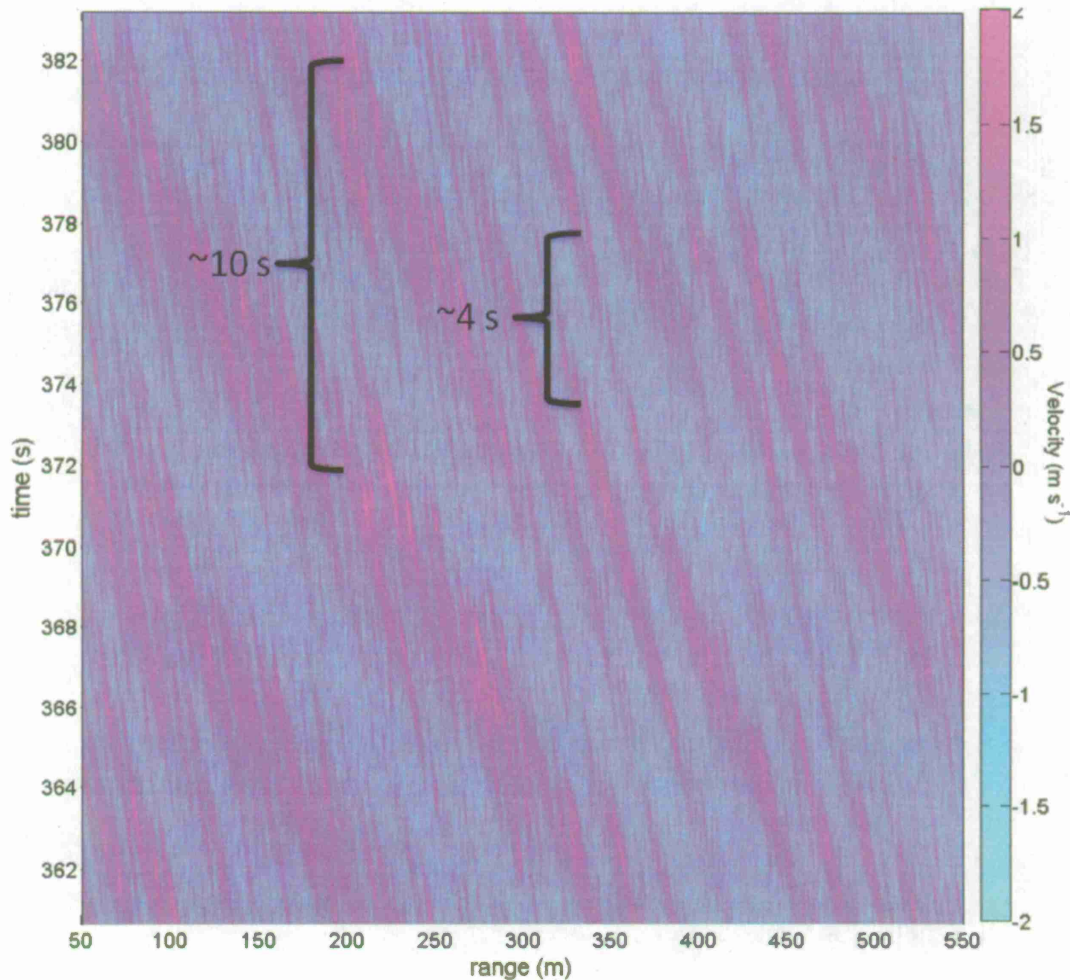


Figure 4. Sample spatiotemporal image of VV Doppler velocity with the mean value removed. Data is for run 246.

The Doppler velocities are downsampled in time to a 0.25 s sampling rate, and detrended along time and range. A 2-D FFT is applied in blocks of 128 s and 614 m, and the resulting 2-D spectra are averaged over all blocks in each dataset, which ranges from 4 to 11 blocks of 128 s depending on the dataset. The 2-D spectra are then multiplied with a binary dispersion filter, D_k , where the subscript k denotes radian wavenumber:

$$D_k(\omega) = 1 \text{ for } \omega_d - 2\Delta\omega < \omega < \omega_d + 2\Delta\omega \quad (2)$$

$$D_k(\omega) = 0 \text{ otherwise}$$

where, ω is the radian frequency, $\Delta\omega$ is radian frequency resolution (here, 0.05 rad s^{-1}), and ω_d is defined by the linear dispersion relationship for surface gravity waves including a current:

$$\omega_d = u_c k + [gk \tanh(kh)]^{1/2} \quad (3)$$

where, u_c is the current speed, taken here to be 3% of the wind speed, g is acceleration due to gravity, k is the radian wavenumber, and h is water depth. A sample averaged 2-D spectrum both before and after filtering are shown in Figure 5. The dashed line in the figures is equation (3), and clearly the largest amount of energy lies along the dispersion curve. In Figure 5a, the line at frequencies above those associated with the dispersion curve that starts at $\sim 0.5 \text{ rad m}^{-1}$ is generally associated with the first harmonic of the surface waves. The broadband signal that starts at low frequencies and wavenumbers is generally referred to as the “group line” because it is conjectured to be associated with wave grouping, but cannot be explained solely by the difference component of the wave field [21]. Other aspects speculated to contribute to this broadband signal include shadowing and breaking waves; however, a clear understanding of this feature remains a topic of current research. The dispersion curve filtering retains the linear portion of the surface wave field and discards all the other energy as shown in Figure 5b. For this low sea state data, exclusion of non-linear aspects of the wave field may not have a significant effect on the results, but at higher sea states this may no longer be valid.

The averaged filtered 2-D spectrum is then integrated over all (radian) frequencies to obtain a 1-D wavenumber spectrum. The final step involves converting the velocity spectrum to a wave height spectrum using a transfer function based on linear wave theory. The full linear relationship between a wave height spectrum and a velocity spectrum is:

$$F_v(k) = \int_0^{2\pi} \frac{g^2 k^2 \cosh^2[k(h+z)]}{\omega^2 \cosh^2(kh)} F_{\eta\eta}(k) D(\theta) \cos^2(\theta - \theta_r) d\theta \quad (4)$$

where, D is a directional distribution, θ is the direction of wave propagation, θ_r is the radar look direction, and z is the vertical coordinate, which is defined as zero at the mean free surface. Subscript vv indicates a velocity spectrum, while $\eta\eta$ indicates a sea surface elevation spectrum. Assuming that the measurements were performed at the surface (i.e., $z = 0$), neglecting directional effects, including assumption that $\theta - \theta_r = 0$, and use of the still-water dispersion relationship, results in the following simplified expression:

$$F_v(k) = \frac{\omega^2}{\tanh^2(kh)} F_{\eta\eta}(k) \quad (5)$$

This relationship is the transfer function used to convert between velocity and sea surface elevation spectra. For comparison with the spectra based on the conventional sensor measurements, the elevation spectra as a function of wavenumber are converted to frequency spectra using:

$$F(k) = F(\omega) c_g \quad (6)$$

where, $F(k)$ and $F(\omega)$ represent power spectral density (PSD) as a function of wavenumber and radian frequency, respectively, and c_g is the group velocity. The group velocity is computed as

$c_g = d\omega/dk$, using the still-water dispersion relationship. Note that integrating the filtered 2-D velocity spectra over wavenumber, then applying the transfer function yields the same result.

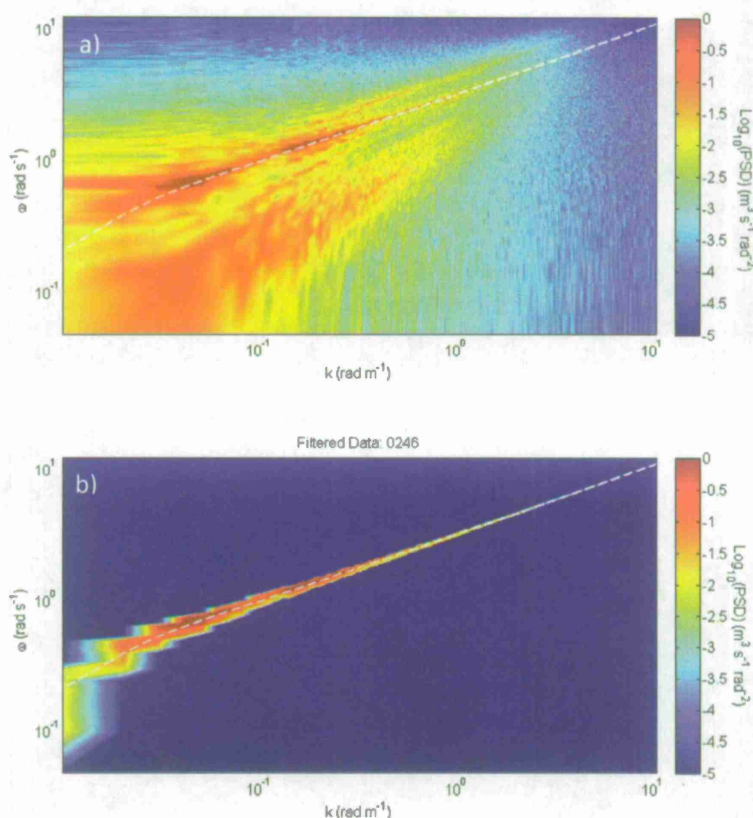


Figure 5. Average 2-D power spectral density of VV Doppler velocities a) before dispersion curve filtering, and b) after filtering (Eqn. 2). The dashed white line is the dispersion relationship for surface gravity waves (Eqn. 3). Data is for run 246.

RCS-BASED SEA SURFACE ELEVATION SPECTRA

The mean squared magnitude over 256 sweeps is computed (after range-resolving the data) with approximately 20% overlap for consecutive averages. Note the length of the average is consistent with that used for processing the Doppler velocities (0.32 s). Sample spatiotemporal images of RCS for VV and HH are shown in Figure 6. This figure shows the RCS values for the same time period as that shown for the Doppler velocities in Figure 4. The correlation between the Doppler velocities and VV RCS is clear. The HH RCS also shows the same pattern but with much less continuity along the wave fronts. Note that the horizontal lines in Figure 6 are due to interference from other radars operating in the vicinity.

In the same manner as the Doppler velocities, a 2-D FFT is applied in sets of 128 s and 614 m, and the mean PSD is subsequently computed. These spectra are filtered using the linear dispersion relationship, equations (2) and (3), and integrated over (radian) frequency. The spectra are then rescaled based on the variance of the wave height spectra computed from the Doppler velocities, i.e.,

$$\tilde{F}_{\eta\eta}(k) = \frac{\xi_{\eta\eta}^2}{\xi_{RCS}^2} F(k) \quad (7)$$

where, $\xi_{\eta\eta}^2$ is the variance associated with the sea surface elevation spectrum computed from the Doppler velocities, $F(k)$ is the PSD of RCS, and ξ_{RCS}^2 is the variance of the RCS spectrum. Finally, the elevation spectra are converted from a function of wavenumber to a function of frequency using (6) (in the same manner as the Doppler spectra). As with the Doppler spectra, if the filtered 2-D PSD is originally integrated over wavenumber rather than frequency and then rescaled using (7) the same result is obtained. A comparison between VV RCS wave height spectra computed by first integrating the filtered 2-D PSD over wavenumber and by first integrating the 2-D filtered PSD over radian frequency is shown in Figure 7. They clearly agree. The discrepancy at the lowest frequencies is associated with differences in the low frequency limit of the data (i.e., the effect of detrending the data), which is lower for the data first integrated over wavenumber. In other words, the wavelength resolved by 128 s is longer than 614 m. For purposes of comparison, it is truncated in the figure so that the low frequency limits match.

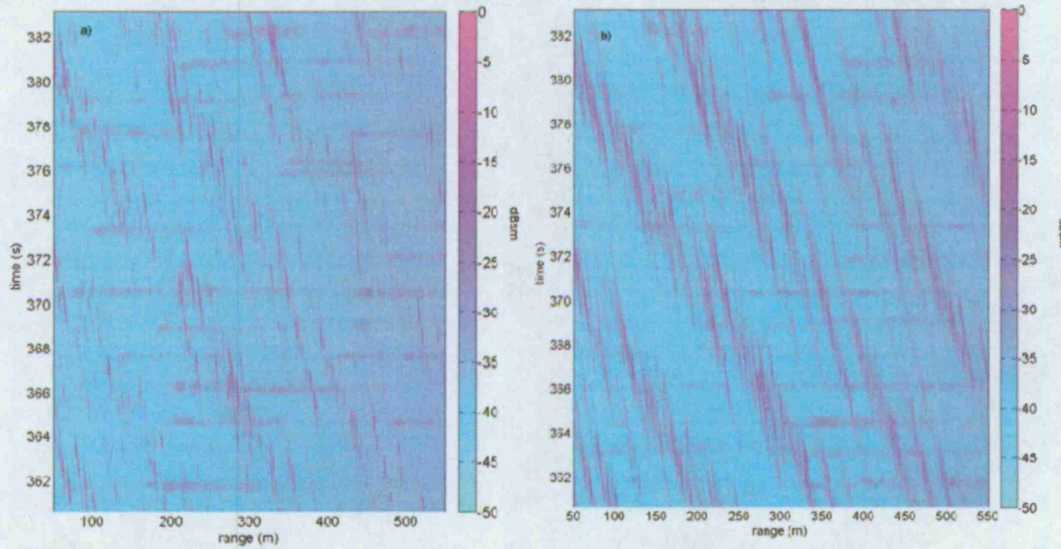


Figure 6. Spatiotemporal image of a) RCS for HH polarization and b) RCS for VV polarization for the same time period as Figure 4.

RESULTS

In this section, comparisons between RCS and Doppler velocities are examined in both spatiotemporal and Fourier domains. In addition, we compare and discuss differences between the spectra obtained with the conventional sensors and that obtained with the radar, including computed wave statistics. For RCS, spectra are computed for both VV and HH polarizations for comparisons. These comparisons show that the VV polarization data more closely match the wave field, so only the VV Doppler data are shown here. The better correlation between ocean waves and intensity fluctuations for VV in comparison to HH, particularly in low sea states, has been noted previously by several authors [e.g., 3, 22-23].

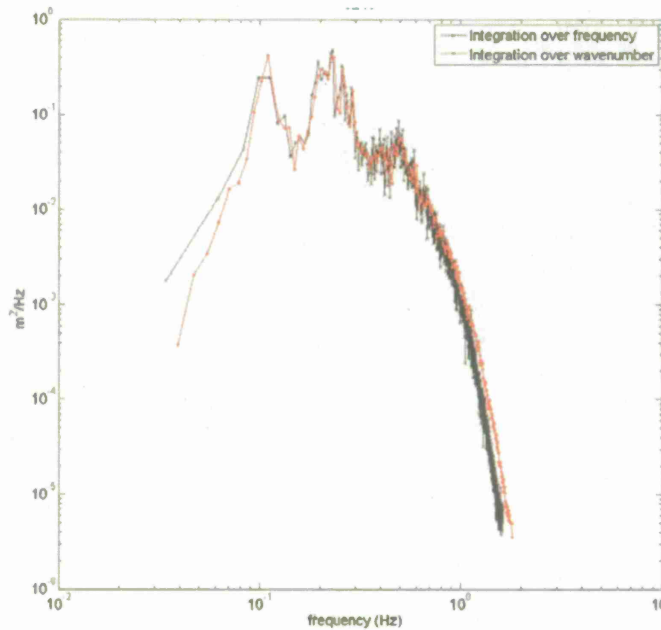


Figure 7. Comparison of VV RCS-based wave height spectra computed from 2-D spectra that were first integrated over radian frequency or first integrated over wavenumber to obtain 1-D frequency spectra.

DOPPLER AND RCS COMPARISONS IN THE SPATIOTEMPORAL DOMAIN

Tilt modulation theory implies that the maximum RCS, σ , should occur near maximum wave slope. Assuming that the detrended Doppler velocities, v , are mostly attributable to the wave orbital velocities, then the maximum Doppler velocities should be observed at the wave crest. By this logic, peak RCS values should lead the peak Doppler velocities by about 90 deg in phase (approximately a quarter of the peak wave period). However, by visual comparison of Figures 4 and 6, it does not appear that there is a phase lag. To examine the relationship between RCS and Doppler modulations, cross-correlation functions are computed. Note that mean values from both the Doppler and RCS time series are removed prior to computing correlation functions. Correlation functions are normalized such that auto-covariances at zero lag are unity, more specifically:

$$\begin{aligned}
 R(m) &= \frac{\sum_{n=1}^{N-|m|} v_{n+m} \sigma_n}{\left[\sum_{n=1}^N v_n v_n \sum_{n=1}^N \sigma_n \sigma_n \right]^{1/2}} & \text{for } m \geq 0 \\
 R(-m) &= \frac{\sum_{n=1+|m|}^N v_{n+m} \sigma_n}{\left[\sum_{n=1}^N v_n v_n \sum_{n=1}^N \sigma_n \sigma_n \right]^{1/2}} & \text{for } m < 0
 \end{aligned} \tag{8}$$

where N indicates the number of discrete samples, and m is the discrete lag. For this data, $N=99$ and the sample rate, Δt , is 0.25 s. Correlation functions are computed in sets of ~ 25 s ($N\Delta t$) and time-averaged over all sets. This procedure results in a mean correlation function, $\overline{R}(r, m\Delta t)$ where the overbar denotes temporal average, for each range bin. Examination of these functions reveals that erroneous results are obtained at the edges of the range window, thus the first and last 50 range bins are neglected in the subsequent computations and discussion.

If these mean correlation functions are then spatially averaged over range, $\langle \overline{R} \rangle (m\Delta t)$ where the $\langle \rangle$ brackets denote spatial average, then an overall nominal correlation function is obtained. A sample for the dataset shown in Figures 4 and 6 is shown in Figure 8. This nominal correlation function is between VV Doppler and VV RCS for the black curve and between VV Doppler and HH RCS for the red curve. The peak correlation is observed at approximately 0.25 s lag with a correlation coefficient of 0.66 for VV, and 0 s lag and 0.46 for HH. There are also local maxima at approximately 4.5 and 9 s as well. The wind wave period is approximately 4.5 s and the second local maximum is twice the wind wave period. Interestingly, the swell component contributes little to the correlation peaks. Although the swell period is ~ 10 s, other datasets that do not have any swell component still show this secondary peak. Thus, the wind sea contributes more to this secondary peak than the swell component. As shown in the next section, the RCS is not as sensitive to the swell component as the Doppler is; hence, it does not present strongly in the correlation function between RCS and Doppler.

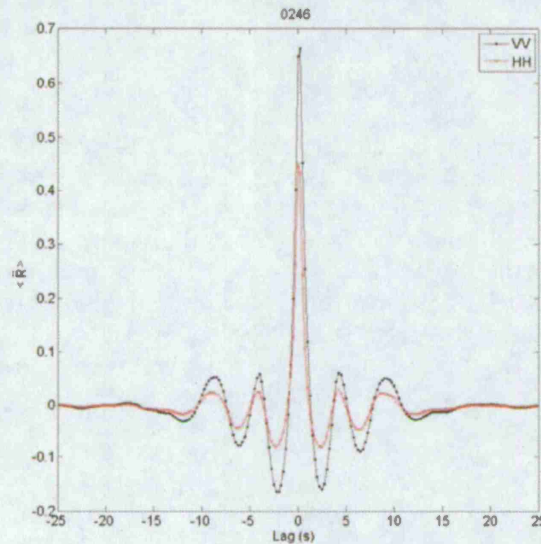


Figure 8. Mean cross-correlation function between VV Doppler velocities and (black) VV RCS and (red) HH RCS for dataset 246.

The approximate zero lag between the Doppler and RCS implies that high Doppler velocities and RCS occur at the same times. This finding contradicts predictions based-on tilt modulation theory, which predicts RCS leading Doppler in the absence of breaking waves, and could be interpreted two ways. One, maximum RCS is occurring very near the crest. If the

Doppler velocities are dominated by orbital velocities, which are highest at the crest, and RCS maxima are in-phase with Doppler maxima, then RCS must also peak near the wave crests. One possible explanation for why it occurs closer to the crest than tilt modulation theory predicts is due to effects of shadowing at low grazing angles, i.e., the RCS modulations due to tilt are not dominant. If shadowing dominates the RCS modulations and the crest is "visible" most often, then on average the 'peak' RCS may be shifted toward the crest. Shadowing has been shown to dominate over tilt modulation at low grazing angles in numerical simulations [2]. The second interpretation is that Doppler-RCS correlation functions could be dominated by (comparatively) few large events, e.g., 'sea-spikes' (although not necessarily only from breaking waves), which result in simultaneous spikes in the Doppler and RCS. These events may not occur as frequently, but may be large enough to dominate the correlation functions. In this case, no conclusion can be drawn as to when in the wave cycle RCS peaks relative to the wave orbital velocities – although most theories regarding the various sources of 'sea spikes' suggest they are also likely to occur near the crest [8-9, 20]. Other data sets provide similar results and the (time and spatial) mean correlation coefficient and lag for each set is provided in Table 2. For VV, on average, the peak RCS leads peak Doppler velocities by 0.17 s, which is less than 5% of the total wave cycle for a 4 second wind-wave period. For HH, the lead is similar but slightly less at 0.13 s. However, the accuracy of the results for the lowest wind speed cases (265 and 267) is insufficient as reflected by their very low correlation coefficients.

Table 2. Maximum and minimum correlation coefficients for all range bins and lags, and overall maximum value and associated lag.

Run	\bar{R}_{\max} VV	\bar{R}_{\max} HH	\bar{R}_{\min} VV	\bar{R}_{\min} HH	$\langle \bar{R} \rangle_{\max}$ VV	$\langle \bar{R} \rangle_{\max}$ HH	$\langle \bar{R} \rangle_{\max}$ lag VV (s)	$\langle \bar{R} \rangle_{\max}$ lag HH (s)
236	0.69	0.36	0.32	0.06	0.52	0.2	0	0
246	0.74	0.54	0.6	0.32	0.66	0.45	0.25	0
250	0.73	0.54	0.48	0.34	0.65	0.45	0.25	0
252	0.6	0.37	0.16	0.07	0.37	0.2	0.25	0.25
254	0.65	0.3	0.11	0.03	0.4	0.1	0	0
258	0.66	0.38	0.35	0.12	0.55	0.26	0.25	0.25
259	0.73	0.53	0.57	0.32	0.67	0.45	0.25	0.25
263	0.69	0.47	0.55	0.27	0.64	0.38	0.25	0.25
265	0.43	0.14	0.03	0.02	0.2	0.09	0.25	0.5
267	0.42	0.1	0.03	0.02	0.17	0.005	0	-0.25
268	0.63	0.35	0.1	0.03	0.33	0.11	0.25	0.25
269	0.71	0.49	0.51	0.23	0.64	0.39	0	0
272	0.68	0.49	0.43	0.24	0.6	0.39	0.25	0.25

The maximum correlation coefficients, \bar{R}_{\max} , decrease as the range increases although the structure along range varies, as shown in Figure 9. In some cases like Figure 9a, the correlation drops off steadily over range, in other cases the distribution is nearly flat and tails off only at the end of the range window (Figure 9b), while in other cases the drop occurs in the near-range and flattens out far-range (Figure 9c). These inconsistencies are likely to be attributable to

other differences in the conditions such as angles between the radar look direction and the wave propagation direction, wind speed and direction (surface roughness). Nevertheless, the lowest correlations are found at far-range and the largest correlations are observed in the near-range. This result means that the Doppler and RCS modulations are more similar in the near-range than they are in the far-range. The reduction in correlation over range could be associated with shadowing, which impacts RCS more significantly than the Doppler signal [24]; thus, they become increasingly less correlated in the far range where shadowing effects are the most significant. Maximum and minimum correlation coefficients over all lags and range bins are provided in Table 2.

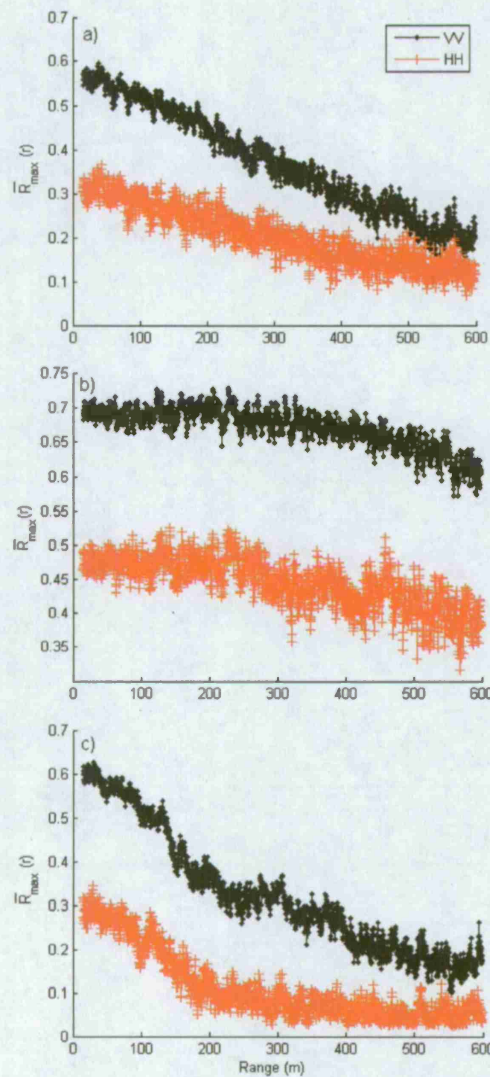


Figure 9. Maximum correlation coefficients between VV Doppler, and (red) HH RCS and (black) VV RCS versus range for datasets (a) 252, (b) 259, and (c) 268.

Not surprisingly, the correlation between VV RCS and (VV) Doppler is much better than it is for HH RCS and (VV) Doppler. This difference is partly attributable to the fact that the Doppler signal is VV, but clearly from the comparison in Figure 6, the HH signal also more poorly aligns with the characteristics (wavelength and period) of the wave field, which also contributes to the lower correlations. As noted previously, the lowest correlation coefficients for both HH and VV occur during the lowest wind speeds (HH correlation values drop to nearly 0). In general, higher correlations were observed during the higher wind speeds, including times with mixed seas. These trends with wind speed are shown in Figure 10.

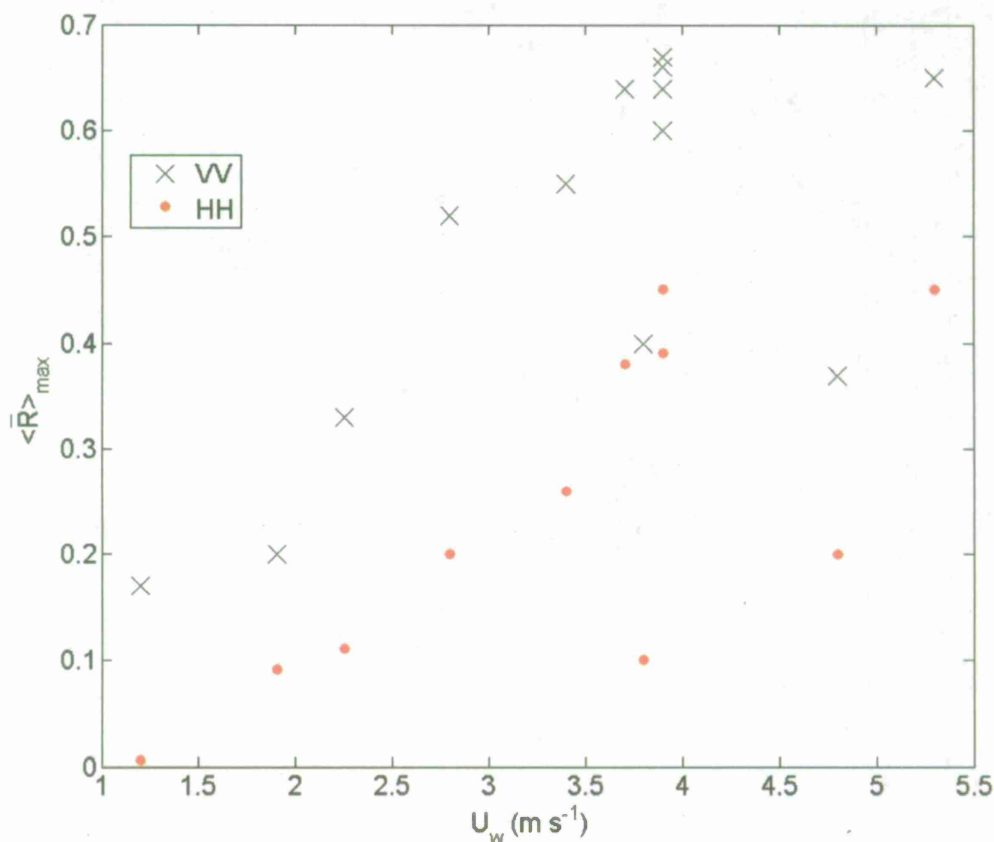


Figure 10. Nominal correlation coefficient between VV Doppler, and VV and HH RCS versus wind speed.

DOPPLER AND RCS COMPARISONS IN FOURIER DOMAIN

Sea surface elevation spectra are computed using the procedures described in the Methods section. In this section, we compare the shapes of these spectra. Although RCS- and Doppler-based spectra contain the same total amount of variance because the RCS transfer function is based-on the Doppler measurements, how the energy is distributed over frequency is not the same. Figures 11, 12, and 13 show VV Doppler, HH RCS, and VV RCS spectral comparisons for all datasets obtained. Based on the buoy and ultrasonic senix array data, which is further discussed in the next section, swell periods were typically of approximately 10 s period, while the wind seas had a period of about 4 s. Aside from the lowest wind speed cases (Figure 13

- 265 and 267; $U_w < 2 \text{ m s}^{-1}$), the energy levels at the wind wave peaks are similar for HH and VV RCS as well as Doppler spectra. However, the HH RCS spectra show slightly less energy than the VV RCS and Doppler in many instances.

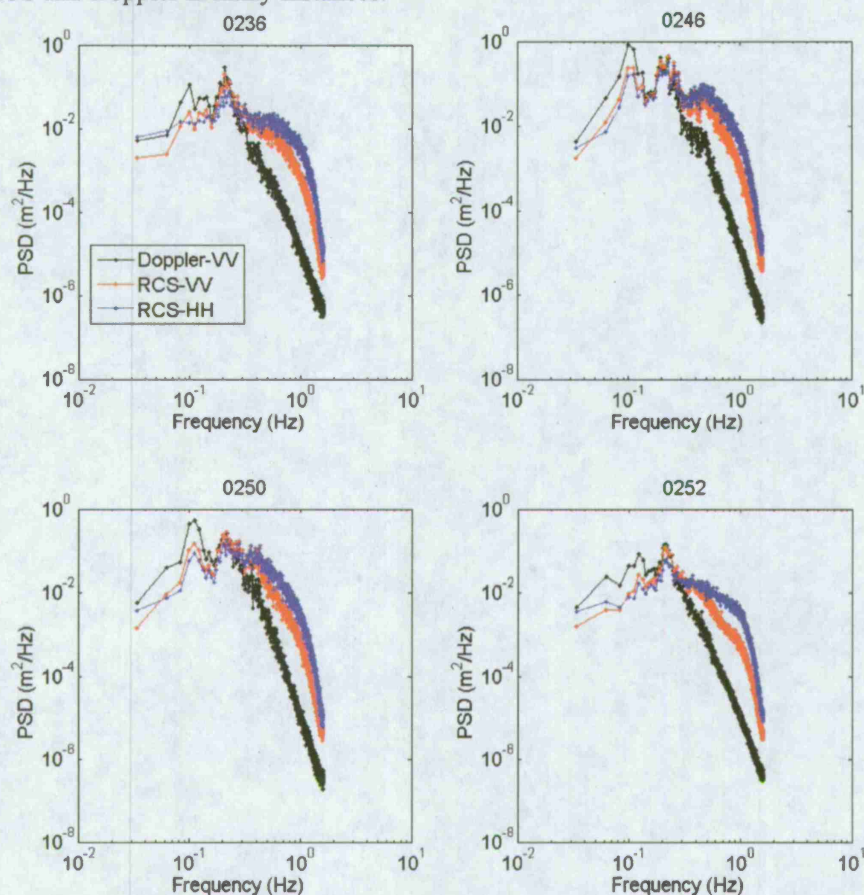


Figure 11. Spectral comparisons between Doppler- and RCS-based sea surface elevation spectra for datasets 236, 246, 250, and 252 (dataset denoted in each subfigure title).

The striking differences between the distributions occur at the swell peak and at frequencies above the wind wave peak. The Doppler spectra show more energy at the swell peak than either RCS measurement. This discrepancy is likely why Doppler-RCS correlation functions do not show a peak at the swell period. In fact, in a number of cases (e.g., Figure 12) essentially no swell peak is represented in the RCS measurements relative to the Doppler. The RCS data is not modulated enough by the swell for its signature to appear in the RCS spectra.

In contrast, there is much more energy at high frequencies in the RCS-based spectra than in the Doppler spectra. The Doppler spectra show a clear roll-off following the wind wave peak. The power-law exponent of this roll-off is less than -5, consistent with a lack of a fully-developed sea. The RCS spectra on the other hand flatten out after the wind wave peak (or roll-off very slowly) followed by a sudden and sharp decrease at the highest frequencies. In dataset 246

(Figure 11), there is even another peak in the RCS data at ~ 0.5 Hz. This second peak may be the first harmonic of the wind sea peak because they are separated by approximately a factor of 2, but due to the width of the spectral peaks it is unclear. The Doppler-based spectra for this run also show a slight flattening of the spectra there. This high frequency contribution demonstrates a much higher sensitivity of the RCS to small-scale modulation factors.

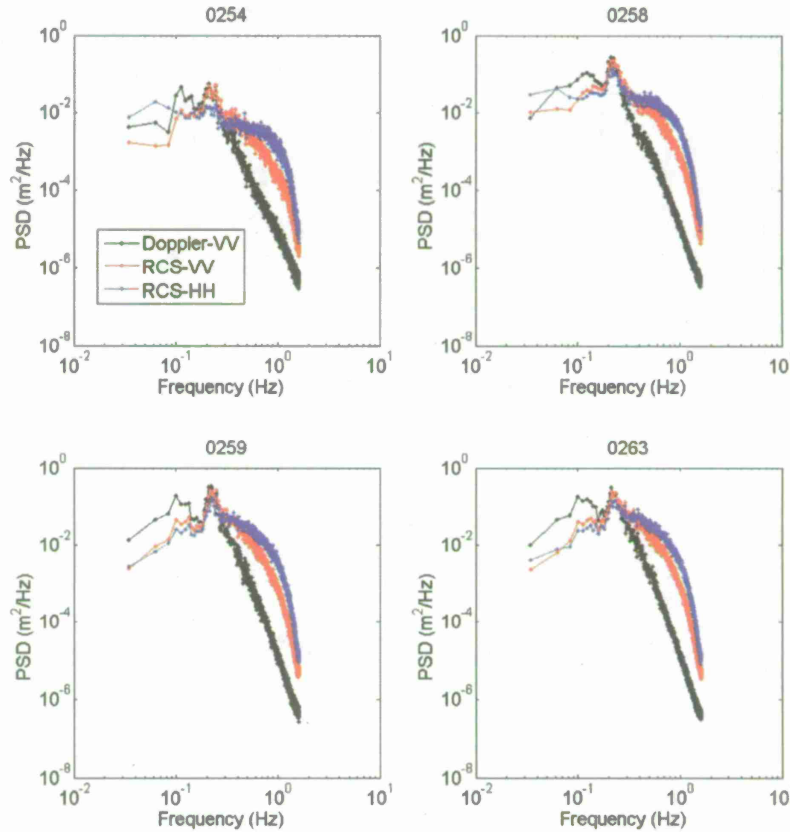


Figure 12. Spectral comparisons between Doppler- and RCS-based sea surface elevation spectra for datasets 254, 258, 259, and 263 (dataset denoted in each subfigure title).

At the lowest wind speeds (Figure 13 – 265 and 267; $U_w < 2 \text{ m s}^{-1}$), the HH RCS spectra clearly no longer reflect any characteristic of the wave field. The VV RCS and Doppler match reasonably well for $U_w = 1.9 \text{ m s}^{-1}$ (Figure 13 – 265), but the VV RCS degrades relative to the Doppler at $U_w = 1.2 \text{ m s}^{-1}$ (Figure 13 – 267). However, as shown in the next section, even the Doppler spectra underestimate the true wave spectral density at these low wind speeds. Nonetheless, the (VV) Doppler and VV RCS appear to characterize the wave field better than HH RCS at low wind speeds.

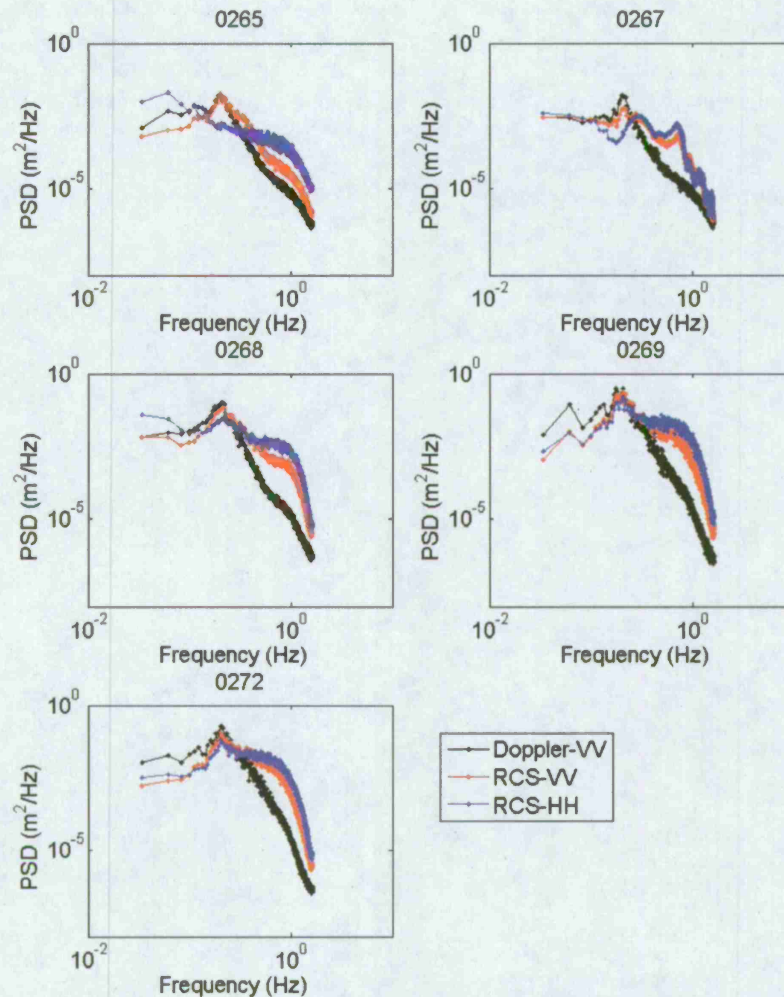


Figure 13. Spectral comparisons between Doppler- and RCS-based sea surface elevation spectra for datasets 265, 267, 268, 269, and 272 (dataset denoted in each subfigure title).

COMPARISON WITH CONVENTIONAL SENSOR DATA

After discussing and examining the differences between RCS and Doppler-based radar spectra, we now show how these spectra compare to wave height spectra measured by the conventional sensors, an ultrasonic Senix wave height sensor array and wave buoy. Because both the spatial and Fourier-based comparisons of the RCS spectra demonstrate that the VV data better represents the characteristics of the wave field, only VV RCS data is shown and discussed in this section (along with the VV Doppler data).

First, comparisons between the radar-based spectra and those obtained with the conventional sensors are examined. For each radar dataset, the measurement acquired by each conventional sensor at the time closest to that of the radar measurements is used for comparison. Due to logistics associated with buoy deployment and recovery, and small boat positioning, as

well as differences in sampling rate, the timing of the conventional sensor measurements differ by as much as a couple hours from that of the radar measurements; however, the majority are within 30 minutes of the radar measurements. For the reader's reference, the times of the conventional sensor measurements and radar measurements are provided in Table 3. In some cases the same conventional sensor measurement is used for comparison with different radar datasets because the conventional sensor sampling rate was comparatively sparse. Both conventional sensors performed measurements less than 1 nmi from the location of the radar measurements. The Senix array spectra are 5-10 min averages, the buoy data 20 min averages, and the radar data 10-20 min averages. The differences between the conventional sensor measurements provide an indication of the spatial and temporal variability of the wave field.

Table 3. Date and time of radar, buoy, and Senix array wave measurements that are used for comparisons. All times are in UTC.

Run	Date	Radar	Buoy	Array
236	7/27/10	17:18	21:03	19:53
246	7/27/10	21:34	21:34	21:44
250	7/27/10	23:26	22:35	22:46
252	7/28/10	17:09	17:31	16:59
254	7/28/10	18:29	18:32	16:59
258	7/28/10	19:47	20:03	20:04
259	7/28/10	20:43	21:04	20:44
263	7/28/10	22:30	22:04	22:24
265	7/29/10	15:49	18:31	17:50
267	7/29/10	18:06	18:31	18:25
268	7/29/10	18:54	18:31	18:25
269	7/29/10	20:22	21:04	20:31
272	7/29/10	21:38	21:04	21:16

Figures 14, 15, and 16 show comparisons of the spectra. Because of the differences in sample rate and sample duration, the spectra have different resolutions, low frequency and nyquist limits. Thus, only the frequency range that all spectra have in common is shown in the figures. The fact that the spectra of the two conventional sensors do not match precisely suggests spatial and temporal inhomogeneity of the wave field, which is not unusual for natural wave fields. For the majority of the datasets, the Doppler-based spectra compare better than the RCS spectra to the conventional sensor data. In two cases, 246 and 250 (Figure 14), the Doppler overestimates the swell energy. Aside from these two cases, the Doppler captures the swell energy much better than the RCS measurements. For three datasets, 254 (Figure 15), 265 and 267 (Figure 16), both the Doppler and RCS compare poorly with the conventional sensor data. The latter two are not surprising as the wind speed was very low ($U_w < 2 \text{ m s}^{-1}$) and the lack of surface roughness greatly degraded the quality of the signal. As the winds picked up (Figure 16: 268, 269, and 272), both RCS and Doppler wind wave peak energy increased to match the array and buoy data, and only the Doppler started to pick up a weak swell as well. For run 254, the radar look direction was significantly offset from the wave propagation direction ($\sim 67^\circ$, see Table 1), and consequently, the Doppler spectral energy is adversely impacted. Recall the

variance of the RCS spectra is based on the Doppler spectra so the RCS will not contain more total energy than the Doppler.

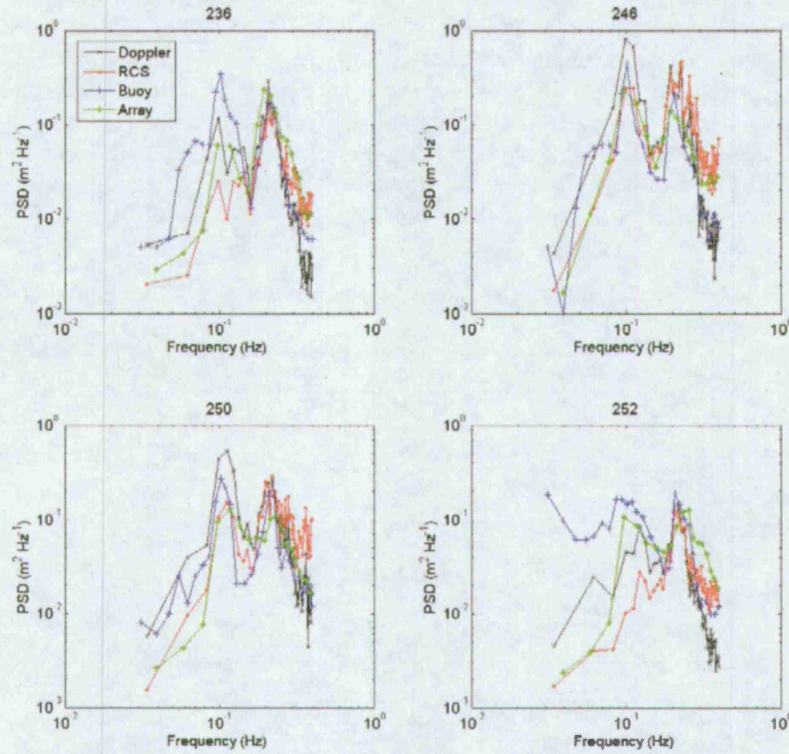


Figure 14. Comparison of buoy, (Senix) array, Doppler, and RCS wave height spectra for runs 236, 246, 250, and 252 (dataset denoted in each subfigure title).

After these general observations, we now compare wave statistics computed from these spectra. First, we examine wave period statistics. Three measures of the wave period are used, peak period, T_p , mean period, T_1 , and zero-crossing period, T_2 , which are defined as follows:

$$T_1 = \frac{\int_{f_1}^{f_2} S(f) df}{\int_{f_1}^{f_2} f S(f) df} \quad (9)$$

$$T_2 = \frac{\int_{f_1}^{f_2} S(f) df}{\int_{f_1}^{f_2} f^2 S(f) df} \quad (10)$$

where, $S(f)$ is the PSD of wave height, and f is linear frequency. The limits of integration, f_1 and f_2 , are chosen to be the same as those presented in Figures 14-16, i.e., only over the region where the frequency range of the various sensors overlap. The peak period is computed as the inverse of the frequency associated with the maximum PSD.

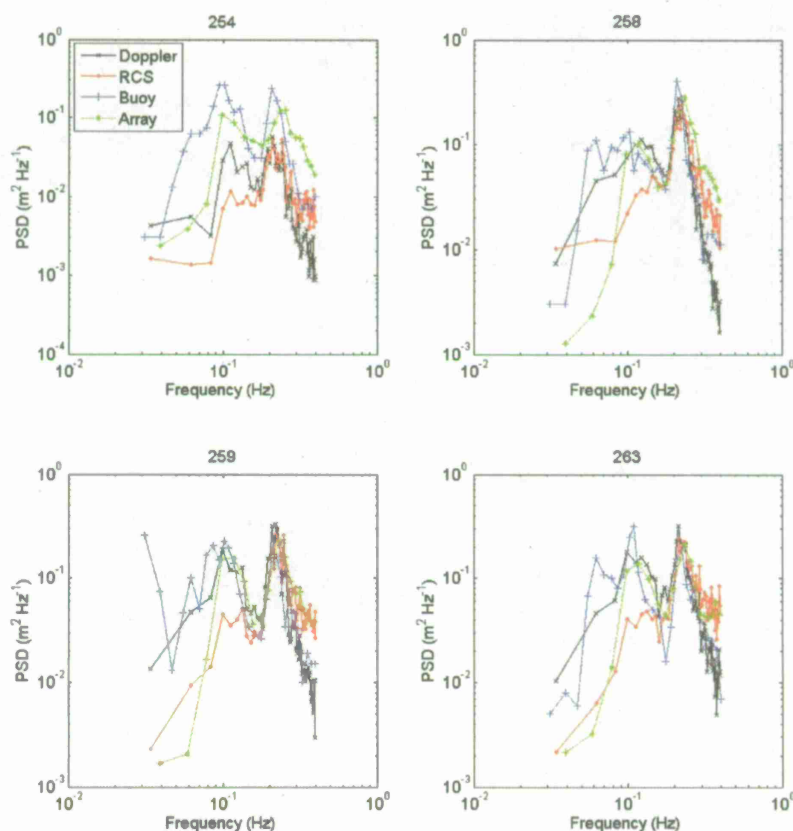


Figure 15. Comparison of buoy, (Senix) array, Doppler, and RCS wave height spectra for runs 254, 258, 259, and 263 (dataset denoted in each subfigure title).

Because data points are taken at slightly different times, it is convenient to first examine a comparison of the time histories of these parameters, Figure 17. As expected, the RCS-based spectra never found a peak period associated with the swell. The Doppler results for peak period are consistent with the array values, while only the buoy identified swell as the peak period for some of the runs on the second day. For both the zero-crossing and mean period, the buoy and Doppler data agree, while the RCS and array data agree. The spectral shapes in the high frequency region of the spectrum (frequencies higher than that associated with the wind wave peak) are similar for the buoy and Doppler, and likewise for the ultrasound array and RCS measurements (Figures 14-16). Higher-order moments such as T_1 and T_2 are influenced by the high frequency portion of the spectrum; thus, these couplings in the period statistics are not surprising. The mere size of the buoy makes it less accurate in responding to high frequency content, and as discussed in the previous section the Doppler signal is less sensitive to small-scale modulations relative to RCS. The slightly lower T_1 and T_2 values of the RCS and ultrasound array relative to the buoy and Doppler are due to the formers' larger energy levels at high frequencies.

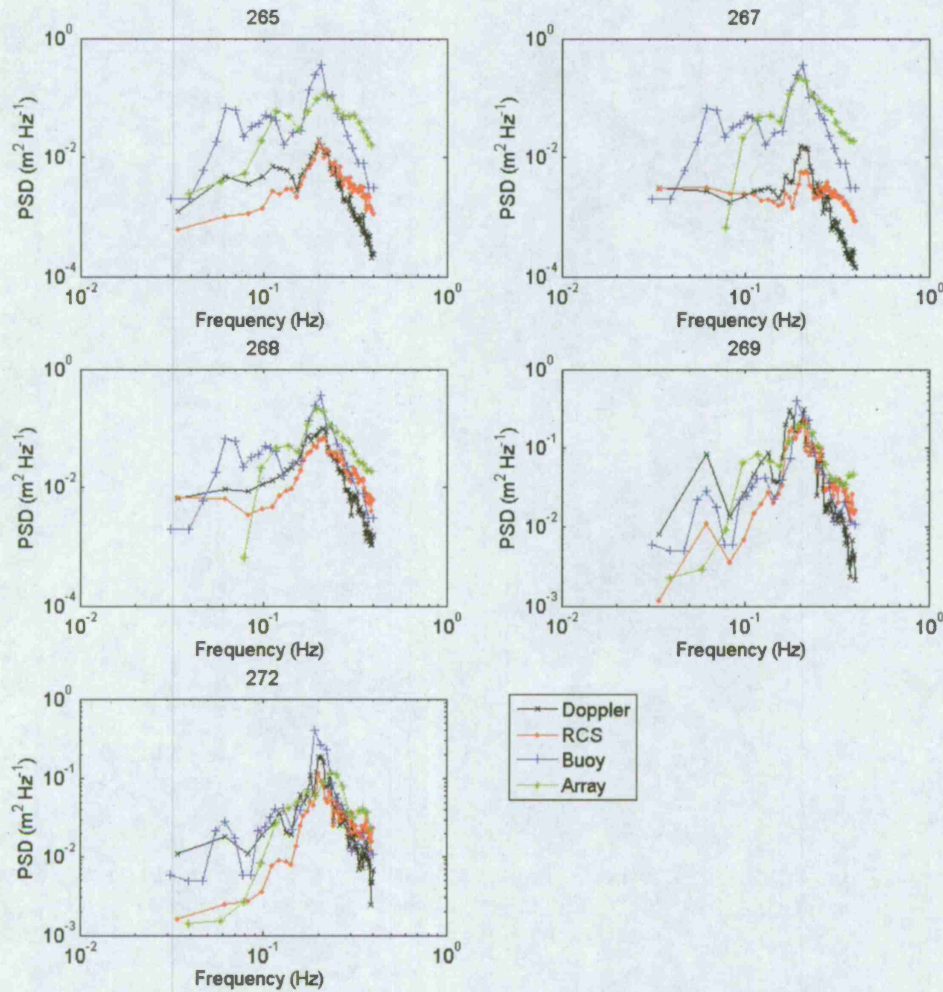


Figure 16. Comparison of buoy, Senix array, Doppler, and RCS wave height spectra for runs 265, 267, 268, 269, and 272 (dataset denoted in each subfigure title).

To examine the differences in more detail, Figure 18 shows the difference between the value measured by the buoy and that measured with the other sensors, denoted by a Δ , e.g., $\Delta T_p = T_p(\text{buoy}) - T_p(\text{other sensor})$. Note that this notation is used consistently with other statistics as well. The buoy is used as the primary point of comparison because it is the most established sensor used, and spectra are obtained from the longest time average. Mean and RMS values of these differences are provided in Table 3. Clearly, the large difference magnitudes for the peak period result from the buoy detecting swell as the dominant wave system as opposed to the wind seas. Thus, for all the Doppler (and all but two datasets for RCS), the difference is equivalent to that of the array. The difference magnitudes for T_1 and T_2 span a much smaller range, and the mean differences are essentially zero for the Doppler measurements. The RCS and array have a

positive bias for ΔT_1 and ΔT_2 . The RMS of the differences is similar for all. Thus, overall, the Doppler and array perform similarly for period measurements, and RCS is about the same with a slightly lower accuracy for peak period due to its underestimation of swell energy.

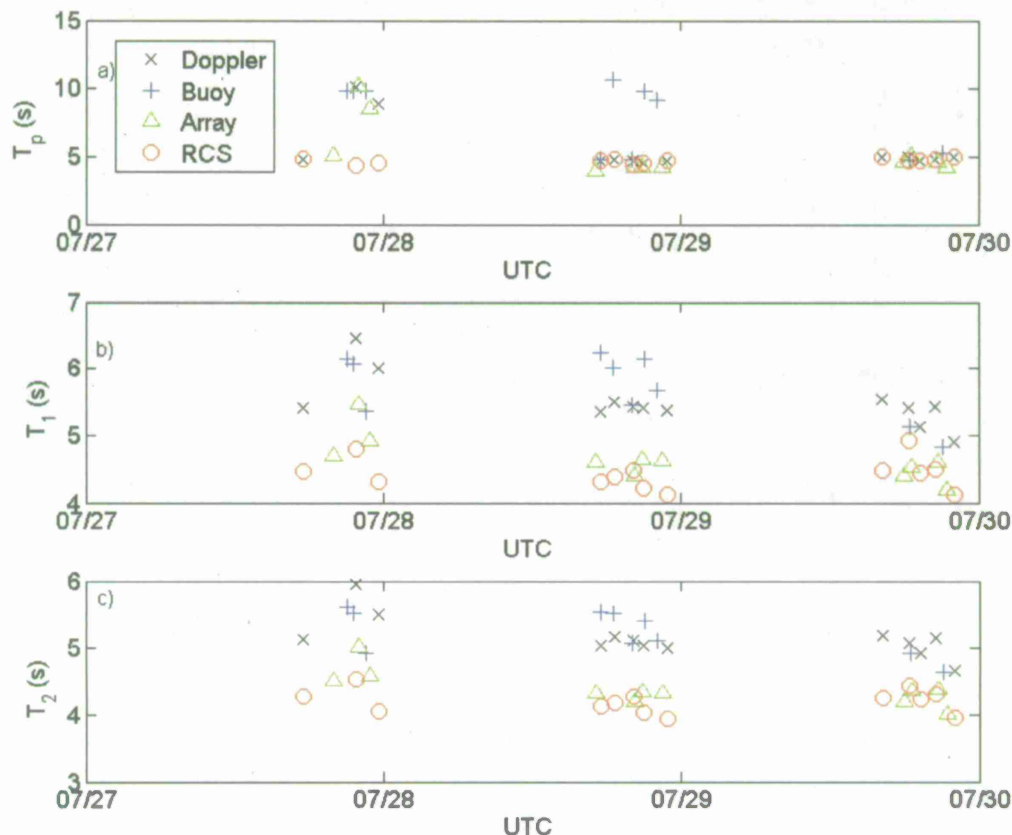


Figure 17. Time histories of (a) peak period, (b) mean period, and (c) zero-crossing period as computed from Doppler-, buoy-, array-, and RCS-based spectra.

Significant wave height is also computed from the spectra using:

$$H_s = 4 \left[\int_0^{\infty} S(f) df \right]^{1/2} \quad (11)$$

Although the Doppler and RCS spectra have the same total amount of variance, the amount of variance over the interval of integration is not the same. Thus, H_s is estimated separately for both the Doppler and RCS data despite their relationship to each other.

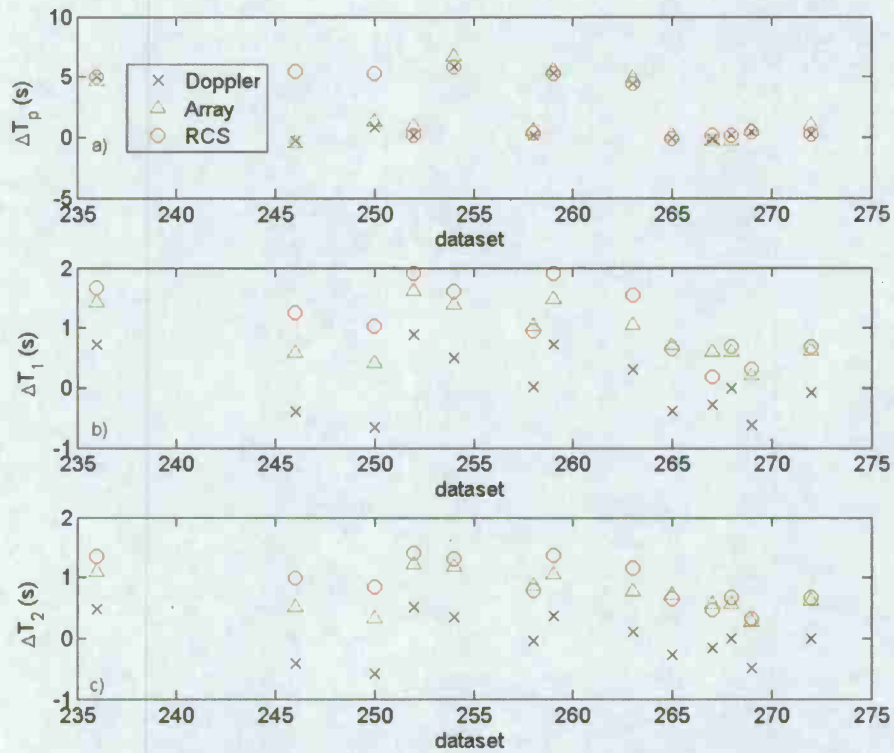


Figure 18. Differences between buoy measured periods and the other sensors for (a) peak period, (b) mean period, and (c) zero-crossing period.

Table 4. Mean and RMS of differences between the buoy measured wave statistics and those measured by the array, Doppler, and RCS.

Statistic	Array	Doppler	RCS
$\overline{\Delta H_s}$ (m)	0.01	0.10	0.15
$[(\Delta H_s)^2]^{1/2}$ (m)	0.05	0.22	0.20
$\overline{\Delta T_p}$ (s)	1.9	1.7	2.5
$[(\Delta T_p)^2]^{1/2}$ (s)	2.4	2.3	2.5
$\overline{\Delta T_1}$ (s)	0.91	0.06	1.12
$[(\Delta T_1)^2]^{1/2}$ (s)	0.44	0.51	0.56
$\overline{\Delta T_2}$ (s)	0.76	-0.01	0.93
$[(\Delta T_2)^2]^{1/2}$ (s)	0.30	0.36	0.35

Figure 19a shows a time history of H_s computed from RCS, Doppler, array, and buoy spectra. There is good agreement between the buoy and array wave height measurements. The radar-based wave heights show much more scatter. It is not surprising that the H_s values are dramatically underestimated for the two low wind speed cases as well as the run with poor alignment with the wave propagation direction (the three lowest values in Figure 19a; datasets 254, 265, and 267). The wave heights are overestimated for two runs when the swell was the dominant wave system (246 and 250). In most of the other cases, the values are reasonable but show much more variability than that measured by the conventional sensors. Differences between the buoy-measured H_s and that measured by the other sensors versus wind speed are shown in Figure 19b, and the mean and RMS of these differences are provided in Table 4. The difference between buoy and array measurements is small with only 5 cm RMS (~8% of the mean H_s over all days). The differences between buoy and radar-based wave height show a strong dependence on wind speed below about 3 m s^{-1} , as shown in Figure 19b, where the differences decrease as the wind speed increases. This behavior is because a minimum amount of surface roughness is necessary to obtain a sufficient radar return signal. Above this threshold, the differences are no longer biased but a large RMS remains. Also, for the majority of the runs the Doppler-based H_s is closer to the buoy measurement than the RCS-based value. Ironically, for the two runs where the swell dominated, the RCS wave height is closer to the conventional measurements than the Doppler despite RCS generally reflecting poorer swell characterization. On average, the radar-based wave heights are underestimated by 10 and 15 cm for Doppler and RCS, respectively, which is an order of magnitude larger than that of the array. The RMS for the Doppler and RCS are 22 and 20 cm, respectively, which is about 4 times larger than that of the array. These RMS values represent about 33% uncertainty on the mean H_s over all days. While these errors may seem large, recall that the sea state was very low, no wave measurement calibration specific to this site was performed, and alignments between the wave propagation direction and the radar look-direction were imperfect. Given these considerations, the errors are reasonable and suggest promise for use of radar as a remote sensing tool over a wide range of conditions without a detailed site specific wave measurement calibration.

SUMMARY AND DISCUSSION

High-resolution (30 cm range bin) radar measurements of the sea surface were performed using a pulse-Doppler system at low grazing angle. Sea surface elevation spectra are computed from both the incoherent and coherent portion of the return signal. For the incoherent return, both VV and HH polarizations are examined. In addition, two conventional sensors measured the seaway nearly simultaneously and in close proximity to the radar measurements. All data were acquired in low sea states, where breaking waves were not a factor in the scattering, and in most cases there were no observable breaking waves. This combination of environmental conditions and radar measurements permits investigation of the differences in retrieved wave information that is associated only with the geometries of and between the ocean and electromagnetic waves, as opposed to effects associated with spray and foam.

Comparisons between HH and VV RCS returns show that at low wind speeds, such as those here, VV modulations better mirror the characteristics of the wave field (e.g., wave period and wavelength). In the most extreme cases where $U_w < 2 \text{ m s}^{-1}$, the HH spectra exhibits no similarity to any characteristic of the wave field, whereas VV is still able to capture correct peak periods despite the limited surface roughness.

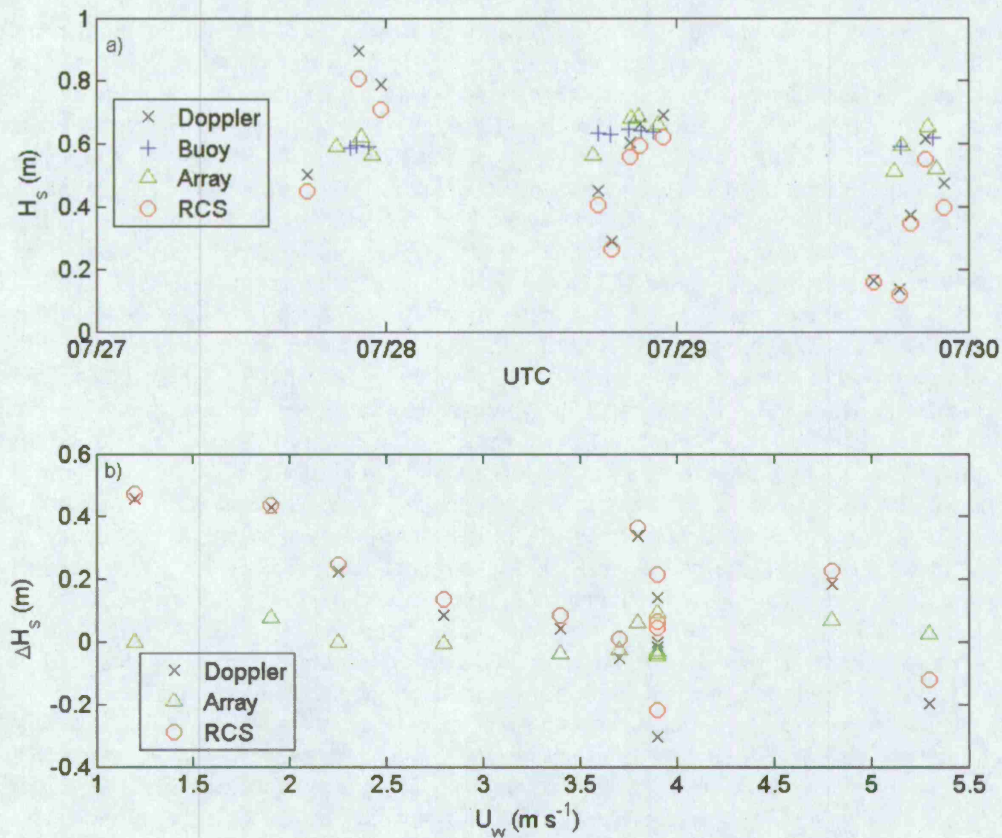


Figure 19. (a) Time history of significant wave height as measured by the buoy, array, Doppler, and RCS. (b) Difference between buoy measured significant wave height and that measured by Doppler, RCS, and ultrasonic array versus wind speed.

Cross-correlation functions between VV Doppler, and HH and VV RCS show that large RCS occur in-phase with large Doppler velocities. This result could suggest that maximum RCS occurs at the crest because if (detrended) Doppler velocities are primarily associated with orbital velocities, then they should be largest at the wave crest. On the other hand, the presence of “sea spikes” that simultaneously result in large RCS and Doppler velocity events could dominate the correlation functions. Because there is essentially no wave breaking for these data sets, the “sea spikes” must be produced by other sources, such as coherent scattering off of intermediate-scale waves [9], wedge scattering from wave facets [8], and/or specular-like returns from specific smaller-scale features on the wave. If these types of scatterers are prevalent in low sea state data, then it is likely in higher sea states that most of the modulations are due to such events including breaking waves, which also cause “sea spikes” [20]. In either case, in-phase Doppler and RCS maxima certainly raise questions about the importance of tilt modulation at low grazing angles. Shadowing, multipath, and “sea spikes” may be dominant over tilt in the modulation of low

grazing angle returns. It should be noted that because this radar has very high spatial resolution in comparison to, for example, a navigation radar, it was possible to track these features through multiple range bins. In contrast, a navigation radar may only sense these features in one bin for a very brief time period. The dominance of shadowing over tilt modulation has been alluded to in numerical simulations [2]. Comparison of Doppler and RCS spectra reveal that Doppler is more sensitive to the swell-induced modulations, while the RCS is more sensitive to high-frequency modulations, and they equally characterize the wind wave peak when there is sufficient surface roughness.

Comparisons of incoherent radar-based wave measurements with buoy data frequently entail intensive site-specific calibrations [25]. These calibrations are often performed with the same instruments that are later used for comparisons. Furthermore, calibration curves need to be established to determine empirical transfer functions to relate signal intensity to wave height for incoherent systems [14]. While these comparisons often reflect good agreements, we must consider practical use of these systems. Ideally, one would like to install radar at various sites or even on a vessel without the requirement of collecting a significant database of information prior to use. In addition, it is well known that even buoys that sample closely in space and time can measure slightly different wave spectra and statistics. This discrepancy is related to the fact that natural wave fields are not stationary or homogeneous. Does it make sense to calibrate radar based on one point sensor, and if not how many are needed, how close together do they need to be, etc.? As this technology progresses, these types of issues need to be addressed.

The comparisons provided here did not rely on any calibration for equating wave height with radar return signal. The transfer functions are based on linear wave theory, as has been done in the past [12, 24, 26-27]. In this study, RCS data are scaled based on Doppler information. Hence, the results presented here have not been "tuned" to the location. Furthermore, the alignment of the radar look direction with the wave propagation direction was imperfect – wave direction was estimated visually and the radar look direction adjusted. The environmental conditions were also not ideal, the sea state was low and in many cases a mixed sea was present; thus, there was more than one wave direction and period. These conditions provide a realistic assessment of the accuracy of radar measurements using the procedures described in the Methods section. Two conventional sensors were also used for comparisons, an ultrasonic wave height array and a buoy. This variety allowed an understanding of the local variability of the wave field to provide a better understanding of how well different measurements should agree given spatial and temporal variations.

Relative to the differences between the conventional sensors, the wave period information obtained from VV Doppler and VV RCS is fairly accurate. The Doppler is slightly better as the RCS did not identify the swell as the peak period in a couple cases. The higher-order moment period statistics, mean period and zero-crossing period, show equivalent accuracy and error (RMS) as the array. The significant wave height comparisons between the array and buoy agree very well (no bias, ~8% error), and the Doppler radar-based estimates showed a ~15% bias, and ~33% uncertainty. RCS values were slightly worse than the Doppler-based estimates. Because the RCS variance is scaled on the Doppler variance, the differences between them for H_s statistics are minimal. Given the low sea state and various misalignments, these results are reasonably promising.

These results provide insight on the characteristics of radar backscatter from the sea surface in low sea states at low grazing angle. Further research investigating and evaluating the various contributors to signal modulations is needed. On-going research focuses on the effects of multipath and evaluation of the relative contribution of it to spatiotemporal modulations.

(THIS PAGE INTENTIONALLY LEFT BLANK)

REFERENCES

- [1] I. R. Young, W. Rosenthal, and F. Ziemer, "A three-dimensional analysis of marine radar images for the determination of ocean wave directionality and surface currents." *Journal of Geophysical Research*, vol. 90, no. C1, pp. 1049-1059, 1985.
- [2] J. C. Nieto Borge, G. R. Rodríguez, K. Hessner, and P. I. González, "Inversion of marine radar images for surface wave analysis," *Journal of Atmospheric and Oceanic Technology*, vol. 21, no. 8, p. 1291-1300, 2004.
- [3] M. W. Long, *Radar Reflectivity of Land and Sea*, Nowood, MA: Artech House, Inc., 385 pp., 1983.
- [4] J.W. Wright, "Backscattering from capillary waves with application to sea clutter," *IEEE Trans. Antennas Propagation*, vol. 14, pp. 749-754, 1966.
- [5] W. Alpers, and K. Hasselmann, "The two-frequency microwave technique for measuring ocean wave spectra from an airplane or satellite," *Boundary Layer Meteorology*, vol. 13, pp. 215-230, 1978.
- [6] D. E. Barrick, "Near-grazing illumination and shadowing of rough surfaces," *Radio Science*, vol. 30, no. 3, pp. 563-580, 1995.
- [7] M. I. Skolnik, *Introduction to Radar Systems*, McGraw-Hill, 3rd Edition, 772 pp, 2001.
- [8] D. R. Lyznega, A. L. Maffett, and R. A. Shuchman, "The contribution of wedge scattering to the radar cross section of the ocean surface, *IEEE Geosci. Remote Sens.*, vol. GE-21, no. 4, pp. 502-505, 1983.
- [9] W. J. Plant, "A model for microwave Doppler sea return at high incidence angles: Bragg scattering from bound, tilted, waves," *J. Geophys. Res.*, vol. 102, no. C9, pp. 21131-21146, 1997.
- [10] G. Soriano, and C. Guerin, "A cutoff invariant two-scale model in electromagnetic scattering from sea surfaces", *IEEE Geosci. Remote Sens. Letters*, vol. 5, no. 2, pp. 199-203, 2008.
- [11] W. J. Plant, W. C. Keller, A. B. Reeves, E. A. Uliana, and J. W. Johnson, "Airborne microwave Doppler measurements of ocean wave directional spectra," *Int. J. Remote Sensing*, vol. 8, no. 3, pp. 315-330, 1987.
- [12] P. A. Hwang, M. A. Sletten, and J. V. Toporkov, "A note on Doppler processing of coherent radar backscatter from the water surface: with application to ocean surface wave measurements," *J. Geophys. Res.*, vol. 115, no. C03026, doi: 10.1029/2009JC005870, 2010.
- [13] O. G. Nwogu, and D. R. Lyzenga, "Surface-wavefield estimation from coherent marine radars," *IEEE Geoscience and Remote Sensing Letters*, vol. 7, no. 4, pp. 631-635, doi: 10.1109/LGRS.2010.2043712, 2010.
- [14] J. C. Nieto-Borge, K. Hessner, and D. D. Mata-moya, "Signal-to-noise ratio analysis to estimate ocean wave heights from X-band marine radar image time series," *IET Radar, Sonar, & Navigation*, vol. 2, no. 1, pp. 35-41, 2008.
- [15] E. E. Hackett, A. M. Fullerton, C. F. Merrill, and T. C. Fu, "Nearshore Sea Clutter Measurements from a Fixed Platform," *NSWCCD Hydromechanics Report*, NSWCCD-50-TR-2012/001, 23 pp., April 2012.
- [16] J. Capon, "High-resolution frequency-wavenumber spectrum analysis," *Proceedings of the IEEE*, vol. 57, no. 8, August, 1969.

-
- [17] D. C. Esteva, "Evaluation of the computation of wave direction with three-gage arrays," U.S. Army Corps of Engineers Technical Paper No. 77-7, 1977.
- [18] T. C. Fu, A. M. Fullerton, E. E. Hackett, and C. F. Merrill, "Shipboard measurement of ocean waves," *Proceedings of the ASME 2011 30th International Conference on Ocean, Offshore, and Arctic Engineering*, Rotterdam, Netherlands, ASME press, 2011.
- [19] D. R. Thompson, and J. R. Jensen, "Synthetic aperture radar interferometry applied to ship-generated internal waves in the 1989 Loch Linnhe experiment," *J. Geophys. Res.*, vol. 98, no. C6, pp. 10259-10269, 1993.
- [20] P. A. Hwang, M. A. Sletten, and J. V. Toporkov, "Analysis of radar sea return for breaking wave investigation," *J. Geophys. Res.*, vol. 113, no. C02003, doi: 10.1029/2007JC004319, 2008.
- [21] W. J. Plant, "Analysis of coherent microwave data collected on the ocean over two decades", *ONR Report*, Grant # N00014-10-10318, 2010.
- [22] L. Cui, Y. He, H. Shen, and H. Lu, "Measurements of ocean wave and current field using dual polarized X-band radar", *Chinese Journal of Oceanology and Limnology*, vol. 28, no. 5, doi: 10.1007/s00343-010-9056-8, pp. 1021-1028, 2010.
- [23] J. G. Boring, E. R. Flynt, M. W. Long, and V. R. Widerquist, "Sea returns study," *Engineering Experiment Station*, Georgia Institute of Technology, *Final Report*, Contract Nobsr-49063, 1957.
- [24] J. T. Johnson, R. J. Burkholder, J. V. Toporkov, D. R. Lyzenga, and W. J. Plant, "A numerical study of the retrieval of sea surface height profiles from low grazing angle radar data," *IEEE Trans. Geoscience and Remote Sensing*, vol. 47, no. 6, pp. 1641-1650, 2009.
- [25] P. Izquierdo, C. Guedes Soares, J. C. Nieto Borge, and G. R. Rodriguez, "A comparison of sea-state parameters from nautical radar images and buoy data," *Ocean Engineering*, vol. 31, pp. 2209-2225, 2004.
- [26] W. J. Plant, W. C. Keller, and K. Hayes, "Simultaneous measurement of ocean winds and waves with an airborne coherent real aperture radar," *J. Atmos. Ocean. Technol.*, vol. 22, no. 7, pp. 832-846, July, 2005.
- [27] S. J. Frasier, Y. Liu, D. Moller, R. E. McIntosh, and C. Long, "Directional ocean wave measurements in a coastal setting using a focused array imaging radar," *IEEE Trans. Geosci. Remote Sens.*, vol. 33, no. 2, pp. 428-440, 1995.

DISTRIBUTION LIST

Copies	Name
1	DTIC
ONR	
5	Patrick Purtell (pdf only), Tom Drake (pdf only), Scott Harper (pdf only), Paul Hess III, Steven Russell
SAIC	
2	Don Wyatt, Kristy Beale, (pdf only)
SIO	
1	Eric Terrill (pdf only)
SCI	
1	Richard Pokrass (pdf only)
CSC	
1	Sarah Richer (pdf only)
Division Distribution	
1	3452 Library (pdf only)
1	5040 Arthur Reed (pdf only)
1	5050 Thomas Fu (pdf only)
1	5800 Rae Hurwitz (pdf only)
3	5830 Erin Hackett, Anne Fullerton, Craig Merrill, (pdf only), Files (2)
1	5510 Christopher Bassler (pdf only)
2	7410 Shaun Simmons, Bruce Crock, (pdf only)
1	7310 Andrew Smith (pdf only)
1	7400 Sung Han (pdf only)